Production efficiencies of $Kr^*(1s_5, 1s_4)$ atoms leading to vacuum-ultraviolet emissions in ac plasma display panels with Kr–Ne binary mixtures measured by laser-absorption spectroscopy

J.-S. Oh and K. Tachibana[a)]
Department of Electronic Science and Engineering, Kyoto University, Kyoto-daigaku Katsura, Nishikyo-ku, Kyoto 615-8510, Japan

H. Hatanaka, Y.-M. Kim, S.-H. Son, and S.-H. Jang
Materials Laboratory, Samsung Advanced Institute of Technology, San 14-1, Nongseo, Giheung, Yongin, Gyeonggi 449-712, Korea

(Received 6 May 2005; accepted 8 October 2005; published online 17 November 2005)

Ne–Kr gas mixtures with high Kr concentrations were applied to ac plasma display panels. Spatiotemporal behaviors of excited Kr atoms in the $1s_5$ metastable state and the $1s_4$ resonance state were measured by microscopic laser-absorption spectroscopy in the binary mixtures with Kr concentrations of 20% and 40%. A systematic comparison was done between the characteristics of Ne–Kr-filled panels and those of conventional Ne–Xe panels with the same structure but with lower Xe concentrations of 5% and 10%. For example, the total number of $Kr^*(1s_5)$ atoms in a unit cell ranged from 7.4×10^7 to 2.0×10^8, at the peak was apparently smaller than the value of $Xe^*(1s_5)$ atoms. However, when the difference in the decay rate of the excited atoms by three-body collision processes is taken into account, the production efficiency of vacuum-ultraviolet (VUV) emission from Kr_2^* excimers is as large as that from Xe_2^* excimers in a usual panel since these processes lead directly to the formation of excimers. From the measured density of $Kr^*(1s_4)$ atoms, it is estimated that the contribution of the atomic resonance line is smaller than the excimer band at those high Kr concentrations. In any case, by summing up those two contributions to the VUV emission, the overall efficiency in the Ne–Kr(40%) panel is estimated to be comparable to that in the Ne–Xe(10%) one. © *2005 American Institute of Physics*. [DOI: 10.1063/1.2131194]

I. INTRODUCTION

Improvement of luminous efficiency is the highest priority issue for plasma display panels (PDPs) to be solved within a few years in a hard competition with liquid-crystal displays (LCDs). Therefore, enthusiastic investigations are progressing in the optimization of the gas compositions as well as the cell structures. At present, binary gas mixtures of Ne and Xe are commonly used in color displays, where the vacuum-ultraviolet (VUV) emission radiated from $Xe^*(1s_4)$ atoms in the resonance state at 147 nm and the molecular band emission from higher vibrational levels of $Xe_2^*(0_u^+)$ excimers at 152 nm and from lower vibrational levels of $Xe_2^*(0_u^+, 0_u^-, 1_u)$ excimers at 173 nm are used to excite the visible phosphors.[1] The effort of efficiency improvement is pointing to the direction of increasing the Xe content in the Ne–Xe binary mixtures[2–7] or employing ternary mixtures with the third additives such as He,[8,9] Ar,[10,11] and Kr[12] as well as increasing the total filling pressure.[6,13] As for the structural issue, several trials are going on by using a longer electrode gap length,[14] making a groove in the dielectric layer in between the sustain electrodes,[15,16] or employing a third electrode for controlling the discharge characteristics.[17]

Going back to the topics on the gas composition in detail, some experimental results have been recently reported that a higher luminous efficiency can be obtained in higher Xe contents (>10%) and at higher pressures (>400 Torr).[7,13] It is also reported that the intensity of the 147 nm line from Xe^* ($1s_4$ in Paschen notation) atoms increases up to 7% and then decreases at higher concentration,[18] while the 173 nm from Xe_2^* excimers increases continuously as the Xe concentration increases from 1% to 30%.[6] However, the experimentally observed total VUV efficiency tends to saturate with Xe concentration over 10%–15%.[4,6] On the other hand, ternary gas mixtures with the addition of He or Ar have been studied for the better efficiency.[8–12,19] It has also been examined that the Ne visible emission decreases when He is added and this leads to an improvement of the color purity.[19]

Alternatively, we have been investigating a possibility of using Ne–Kr binary mixtures with higher Kr concentration up to 50%.[20–22] There are several advantages expected in the Kr mixture: a longer lifetime of a Kr-containing panel due to a lower sputtering rate of the MgO protective layer, a lower operating voltage with the higher secondary-electron-emission coefficient of Kr^+ ions on the MgO layer, and so on. In case of the Ne–Kr mixture, VUV emissions occur at 123.6 nm from $Kr^*(1s_4)$ atoms and at 125.0 nm from higher vibrational levels of $Kr_2^*(0_u^+)$ and 148.0 nm from lower vibrational levels of $Kr_2^*(0_u^+, 0_u^-, 1_u)$ excimers, respectively,[23] although these shorter wavelengths may be disadvantageous for the efficiency of phosphors. In this paper, we investigate electrical characteristics of the discharge in Ne–Kr mixture and spatiotemporal behaviors of excited Kr^* atoms in the $1s_5$

[a)]Electronic mail: tatibana@kuee.kyoto-u.ac.jp

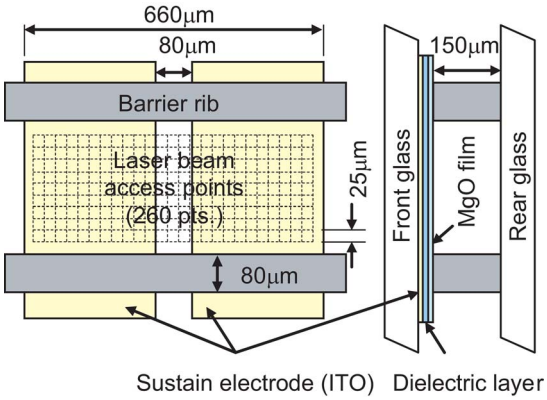

FIG. 1. (Color online) Schematic of the unit cell structure of the test panel and access points for the laser-absorption measurement.

metastable state and the $1s_4$ resonance state using the laser-absorption technique which we have developed previously.[24] Then, we estimate the VUV photon production efficiency from the measured absolute densities of $Kr^*(1s_4, 1s_5)$ atoms and compare the results with those obtained similarly in the Ne–Xe mixture.

II. EXPERIMENTAL SETUP AND PROCEDURE

A. Test panels and experimental setup

We prepared four test panels of 6 in. in diagonal size which contain Ne–Kr(20%), Ne–Kr(40%), Ne–Xe(5%), and Ne–Xe(10%) mixtures, at the same total pressure of 450 Torr. The cell structure is shown schematically in Fig. 1, which is essentially the same as a standard video graphics array (VGA) level structure (1080 μm cell pitch) used in a commercial panel of 42 in. class. There are about 286×84 discharge cells in each test panels. It has a coplanar structure with a pair of indium tin oxide (ITO) sustain electrodes placed on the front glass plate. These are covered successively with a dielectric layer and an MgO layer (about 500 nm thick) to protect the dielectric from sputtering and to provide larger secondary electron emission under ion impacts. The front glass plate is separated from the back one by 150 μm with barrier ribs. As opposed to a conventional cell structure, address electrodes, metallic bus lines for the sustain electrodes, and phosphor layers were removed to allow the optical access by the probe-laser beam. The operating pulses for the sustain discharge were prepared by an arbitrary wave-form generator combined with high-speed voltage amplifiers, of which the pulse width, frequency, and the rise time were 8.4 μs, 30 kHz, and 300 ns, respectively.

The experimental setup of laser-absorption spectroscopy is basically the same as that used previously.[25] In short, we used a tunable semiconductor laser system, which has a coarse tuning range of $\Delta\lambda < 90$ nm and a mode-hop-free piezoelectric fine tuning range of $\Delta\lambda < 0.8$ nm. The laser beam was divided into two parts by a beam splitter. One part was led through a reference discharge tube filled with pure krypton (or xenon) gas at 2 Torr for tuning the wavelength to the absorption peak. The other was led into an optical microscope, where the test panel was mounted on its micropositioning *xyz* stage. The transmitted beam was detected by a photomultiplier through a monochromator at the wavelength of 811.3 nm for $Kr^*(1s_5)$ atoms [or 823.1 nm for $Xe^*(1s_5)$ atoms] in the metastable state and 829.8 nm for $Kr^*(1s_4)$ atoms [or 828.0 nm for $Xe^*(1s_4)$ atoms] in the resonance state. The typical beam diameter was about 15 μm at the center of the gas gap in a discharge panel. The measurement was performed at 26×10 points in the *xy* plane of a discharge cell as shown in Fig. 1. The wave form of discharge current in a line containing 286 discharge cells was measured by a digital oscilloscope using a differential probe though a series resistor of 37 Ω.

Two-dimensional optical emission image was also measured using a gated intensified charge-coupled device (ICCD) camera equipped with a band pass filter centered at 820 nm for observing mostly the near-IR emission corresponding to the transitions from the $2p$ to $1s$ levels of Kr or Xe. The gate width was set at 10 ns and the delay time was scanned to cover the whole emission period in a half cycle of the sustain discharge where one of the sustain electrode was working as the anode and the other as the cathode.

B. Absolute density derivation

The derivation method for the absolute density of excited atoms from the corresponding line absorption data is essential in our work. For the purpose, the spectral profile of those lines should be measured in advance. In the case of natural Xe gas, there exist a variety of isotopes with mass numbers from 124 to 136. Odd-mass-number species exhibit complicated hyperfine structures due to the nonzero nuclear spins, while those with even mass numbers only show small amounts of mass shifts.[26] In the case of Kr, there is only one isotope with odd mass number of 83 and the natural abundance is only about 10%. This makes the line shape much simpler. At the high pressure range used in PDPs, the effect of pressure broadening predominates over the mass shifts of even isotopes, and the measured line shape can be expressed by a Lorentzian profile as shown in Fig. 2. The absorbance at the frequency $\nu=\nu_L$ of the diode laser gives the absorption coefficient $k(\nu_L)$,

$$I = I_0 \exp[-k(\nu_L)d], \tag{1}$$

where I_0 and I are the incident and transmitted laser intensities and d is the absorption length. Thus, the density of atoms N_1 in the lower level 1, i.e., $1s_5$ or $1s_4$ in our case, in the transition to the upper level 2 is obtained by the integration of $k(\nu)$ over the line profile,

$$N_1 = \frac{8\pi g_1}{\lambda_0^2 g_2 A_{21}} \int k(\nu) d\nu, \tag{2}$$

where λ_0 is the wavelength, A_{21} is the transition probability, and g_1 and g_2 are the statistical weights of the lower and upper levels.

If we assume hypothetically a single Doppler profile, the integration of Eq. (1) can be performed analytically as[27]

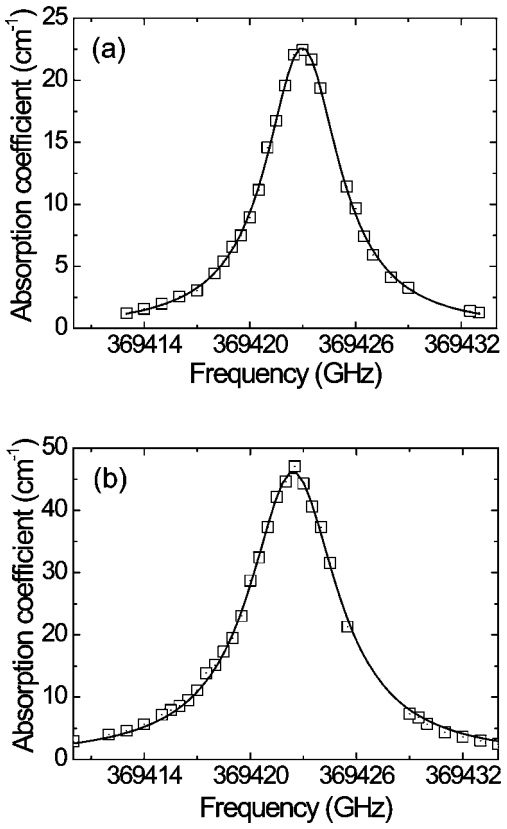

FIG. 2. Absorption line profile of the 811.29 nm transition of Kr measured in (a) Ne–Kr(20%) panel and (b) Ne–Kr(40%) panel.

$$\int k(\nu)d\nu = \frac{\Delta\nu_D}{2}\sqrt{\frac{\pi}{\ln 2}}k_0 = \frac{\lambda_0^2 g_2}{8\pi g_1}A_{21}N_1, \tag{3}$$

with the Doppler width [full width of half maximum (FWHM)]

$$\Delta\nu_D = \frac{2\sqrt{2R\ln 2}}{c}\nu_0\sqrt{\frac{T}{M}}, \tag{4}$$

where R is the gas constant, M is the atomic mass number, and T is the gas temperature. In practice, we fix the frequency at the absorption peak ($\nu=\nu_0$). Therefore, we define the ratio $k(\nu_0)/k_0$ as the correction factor H for the real situation, where $k(\nu_0)$ is the absorption coefficient of the broadened line profile at the peak and k_0 is that of the hypothetical Doppler profile. Here, it is assumed that both profiles are normalized to unity in the integration over the frequency. The values of H for the Kr 811.3 nm line used for the metastable atoms at 450 Torr with the Kr concentrations of 20% and 40% in Ne were derived from the observed line shapes shown in Fig. 2 as 1/12.5 and 1/15.0, respectively. The values for the 829.8 nm line for the resonance atoms are 1/33.4 and 1/52.9, correspondingly. On the other hand, those values for the Xe line at 823.1 nm were 1/20.3 and 1/21.4 for Xe(5%) and those for the 828.0 nm line were 1/38.3 and 1/41.6 for Xe(10%).

Regarding with those absorption line profiles having the pressure-broadened Lorentzian shapes, we estimated the self-broadening coefficient ξ_{Kr} and the foreign-gas broadening coefficient with neon ξ_{Ne}. By neglecting the Doppler width of about 0.5 GHz, the observed linewidth $\Delta\nu_L$ (FWHM) in units of cm^{-1} is given as[28]

$$\Delta\nu_L/c = \xi_{\mathrm{Kr}}N_{\mathrm{Kr}} + \xi_{\mathrm{Ne}}N_{\mathrm{Ne}} = N[R_G\xi_{\mathrm{Kr}} + (1-R_G)\xi_{\mathrm{Ne}}], \tag{5}$$

where N_{Kr} and N_{Ne} are the density of Kr and Ne atoms, $N(=1.45\times10^{19}\ \mathrm{cm}^{-3})$ is the total gas density at the gas temperature of 300 K, and R_G is the concentration ratio of Kr in the Ne–Kr mixture. In principle, ξ_{Kr} and ξ_{Ne} can be obtained according to our measured linewidths at two different gas conditions (20% and 40%), although the procedure only from two data points may include fairly large errors. In any case, the obtained results are $\xi_{\mathrm{Kr}}=1.96\times10^{-20}$ cm^{-1} cm^3 and $\xi_{\mathrm{Ne}}=0.88\times10^{-20}$ cm^{-1} cm^3 for the 811.3 nm line, and $\xi_{\mathrm{Kr}}=10.82\times10^{-20}$ cm^{-1} cm^3 and $\xi_{\mathrm{Ne}}=1.17\times10^{-20}$ cm^{-1} cm^3 for the 829.8 nm line, respectively. It is noticed that the value of ξ_{Kr} for the 829.8 nm line is much larger than that for the 811.3 nm line. It is due to the resonance broadening effect of the former transition which has the $1s_4$ resonance state as the lower level. Similarly, we obtained those coefficients in the Ne–Xe mixture with two different conditions as $\xi_{\mathrm{Xe}}=3.18\times10^{-20}$ cm^{-1} cm^3 and $\xi_{\mathrm{Ne}}=1.41\times10^{-20}$ cm^{-1} cm^3 for the 823.1 nm line, and $\xi_{\mathrm{Xe}}=17.4\times10^{-20}$ cm^{-1} cm^3 and $\xi_{\mathrm{Ne}}=1.53\times10^{-20}$ cm^{-1} cm^3 for the 828.0 nm line, respectively. Those values are consistent with our previously estimated values.[29]

III. RESULTS AND DISCUSSION

A. Spatiotemporal behavior

Figure 3 shows spatiotemporal images of the near-IR emission from Kr$^*(2p)$ atoms in the Ne–Kr(40%) cell observed by the ICCD camera at several values of the sustain voltage V_s. The discharge starts on the edge of the temporal anode and shifts toward the cathode. In the mean time, several striated peaks appear on the anode side and a broad peak on the cathode, expanding toward both ends of the electrodes. At lower V_s the anode peak concentrates at the center of the inner anode edge and the striations spread circularly to outer ribs, but with the increase of V_s the length of the first striation becomes longer to fill the cell width, and the discharge volume on the cathode side also increases rapidly.

Figure 4 shows the corresponding images taken in the Ne–Xe(10%) panel. The characteristic features are the same as those observed previously.[17,25,30,31] A noticeable difference between the Kr- and Xe-filled panels is in the number and the pitch of striations. The reason may be attributed to the different atomic masses and ion mobilities in those gas mixtures in addition to the difference in the partial pressure of Kr and Xe. Spatiotemporal behaviors of IR emission images at lower concentrations of Kr(20%) and Xe(5%) are that the number of the striations becomes smaller and consequently the pitch becomes larger.

Spatiotemporal behaviors of the density of Kr$^*(1s_5)$ atoms in the Kr(40%) and Kr(20%) panels are shown in Fig. 5 in a temporal sequence. Both of them were taken at the same V_s(=230 V). It was observed that in the Kr(40%) panel a sharp peak appeared on the temporal cathode side at 1 μs with a peak density of 2.1×10^{13} cm^{-3}. At the lower Kr con-

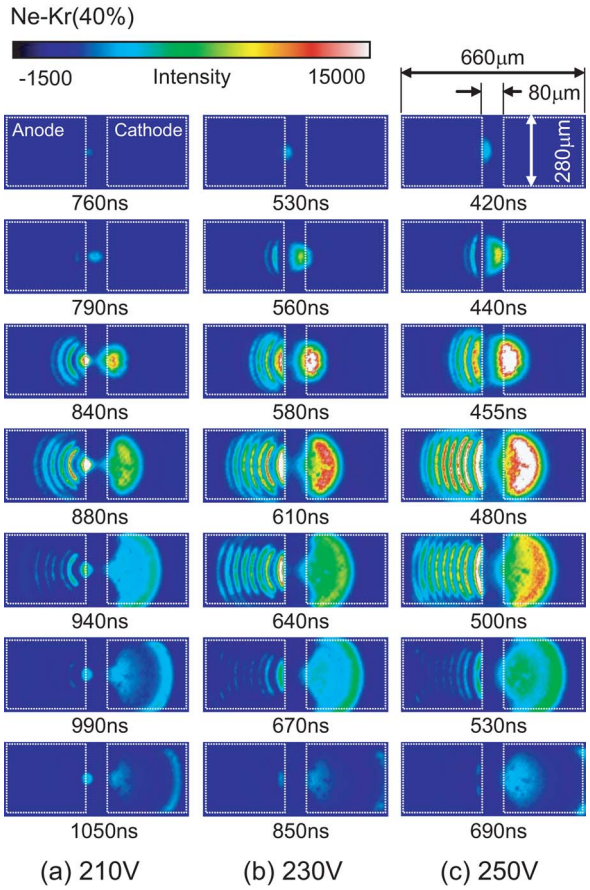

FIG. 3. (Color online) Spatiotemporal behavior of near-IR emission measured in Ne–Kr(40%) panel at sustain pulse voltages of (a) 210 V, (b) 230 V, and (c) 250 V in a half cycle where the left side is working as the anode and the right side as the cathode.

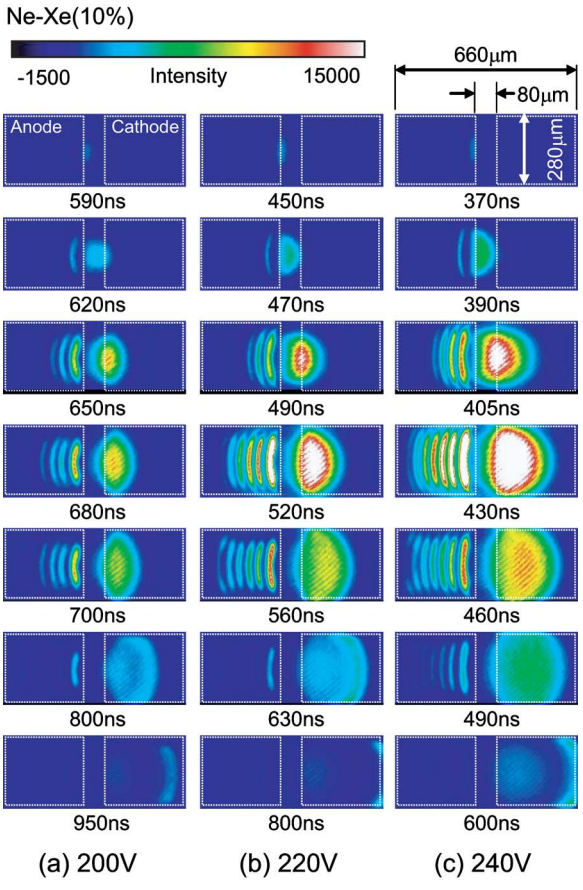

FIG. 4. (Color online) Spatiotemporal behavior of near-IR emission measured in Ne–Xe(10%) panel at sustain pulse voltages of (a) 200 V, (b) 220 V, and (c) 240 V in the same situation as in Fig. 3.

centration, the cathode peak broadened with a lower peak density of 1.4×10^{13} cm^{-3} and the anode peak lengthened but became doubly peaked shape. It is also noted that other two peaks are observed in the Kr(40%) panel at the end of the cathode after 1 μs, which are also seen in the near-IR emission image. The corresponding results on the Xe(10%) and Xe(5%) panels are shown in Fig. 6. The characteristic features and the dependence on the Xe concentration are essentially the same as those in Kr panels except relatively broader density distributions on both the anode and cathode sides. In a quantitative comparison between Figs. 5 and 6, the absolute densities of $Kr^*(1s_5)$ atoms are relatively smaller than those of $Xe^*(1s_5)$ atoms.

Characteristics of the spatiotemporal distributions of $Kr^*(1s_4)$ and $Xe^*(1s_4)$ resonance atoms measured in the four test panels were shown in Figs. 7 and 8, respectively. In comparison with the results of metastable atoms, the density profiles of resonance atoms are alike. However, the peak density is smaller, i.e., of the order of 10^{12} cm^{-3}, and decays much faster. The quantitative analysis will be given below.

B. Decay of excited atoms

Logarithmic plots of the total number of $Kr^*(1s_5)$ atoms $N^*(t)$ in the Kr(20%) and Kr(40%) panels versus time t are shown in Figs. 9(a) and 9(b), respectively. The total number was obtained by integrating the density distribution over the whole volume of a unit cell at each time step [see Eq. (10) below]. Measurements were performed at several values of V_s shown in the insets. The discharge delay time in the Kr(20%) panel is almost independent of the values of V_s used in the experiments, so that the density increases simultaneously up to about 1 μs and decays with the same time constant τ of 1.65 μs (or the decay rate $\gamma=1/\tau$). In the case of the Kr(40%) panel the delay differs with V_s, but the decay time constant is the same for the four different values of V_s within the experimental error as $\tau=0.88$ μs. Figure 10 shows the total number of the $Xe^*(1s_5)$ atoms versus time obtained in the Xe(5%) and Xe(10%) panels. It should be noticed that the relatively large peak values were obtained in the Xe mixtures compared to the Kr mixtures. Correspondingly, the decay time constants are also larger as 2.55 μs for the Xe(5%) and 1.60 μs for the Xe(10%).

We now consider the decay time constants τ of the $Kr^*(1s_5)$ and $Xe^*(1s_5)$ metastable atoms. General models for the decay of those atoms were proposed and analyzed in pure Kr and its mixtures by Turner,[32] Janssens *et al.*[33] Papanyan *et al.*,[34] Aouame *et al.*,[23] and Leichner and Ericson[35] and in Xe by Galy *et al.*[36] and Leichner *et al.*[37] At such a high pressure in the present situation, the three-body collision processes forming Kr_2^* and Xe_2^* excimers are predominant in two pathways: (1) reaction of an excited Kr (or Xe) atom with two Kr (or Xe) atoms in the ground state and (2) reaction with one

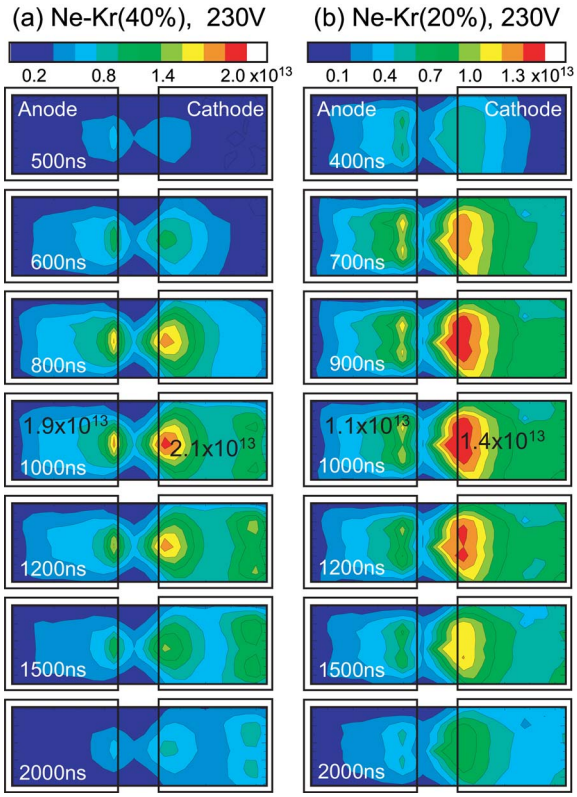

FIG. 5. (Color online) Spatiotemporal behavior of metastable $Kr^*(1s_5)$ atom density (in units of 10^{13} cm^{-3}) measured in (a) Ne–Kr(40%) and (b) Ne–Kr(20%) panels at a sustain pulse voltage of 230 V in a half cycle where the left side is working as the anode and the right side as the cathode.

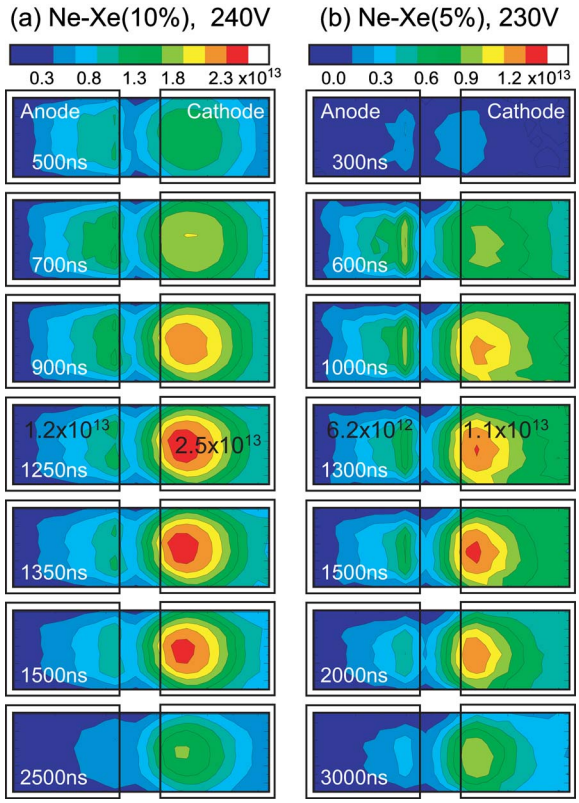

FIG. 6. (Color online) Spatiotemporal behavior of metastable $Xe^*(1s_5)$ atom density (in units of 10^{13} cm^{-3}) measured in (a) Ne–Xe(10%) panel at the sustain pulse voltage of 240 V and (b) Ne–Xe(5%) panel at a sustain pulse voltage of 230 V in the same situation as in Fig. 5.

Kr (or Xe) atom and one Ne atom both in the ground state. When we define the three-body reaction-rate constants for the two pathways as K_1 and K_2, respectively, the decay time constants τ is given by the following equation as

$$1/\tau = K_1 N_{\mathrm{Kr(Xe)}}^2 + K_2 N_{\mathrm{Kr(Xe)}} N_{\mathrm{Ne}} = N^2[K_1 R_G{}^2 + K_2 R_G(1-R_G)]. \quad (6)$$

As in the case of the broadening coefficients described above, we can derive K_1 and K_2, in principle, from the data taken at two different gas conditions. However, the trial procedure yielded erroneous results such as $K_1 < K_2$ in contradiction to previously reported values. It is possibly due to the contribution of other decay processes such as the diffusion loss and the two-body collisional mixing between the $1s_5$ and $1s_4$ levels, of which the effect becomes relatively larger at smaller Kr (or Xe) ratio, making the apparent decay time constant shorter. Therefore, we tried alternatively to estimate the time constants τ by using the reported values and compared the results with our experimental data. When we adapt the values of $K_1 = 2.03 \times 10^{-32}$ cm^6 s^{-1} and $K_2 = 0.77 \times 10^{-32}$ cm^6 s^{-1} given by Aouame *et al.* for the Ne–Kr mixture,[23] the values of τ become 2.33 and 0.94 μs, respectively, for the 20% and 40% Kr concentrations. Our experimental values scatter from 1.43 to 1.94 μs in the former case and from 0.67 to 0.92 μs in the latter case. In both cases the experimental data are smaller than the estimated values and the difference is larger at smaller Kr concentration as suggested from the above argument.

In the case of the Ne–Xe mixture, when we adapt the values of $K_1 = 8.5 \times 10^{-32}$ cm^6 s^{-1} and $K_2 = 1.4 \times 10^{-32}$ cm^6 s^{-1} taken from Galy *et al.*,[36] the estimated values of τ become 5.43 and 2.26 μs for the 5% and 10% Xe concentrations, respectively. Those are fairly larger than the experimental data ranging from 2.5 to 3.3 μs for the former situation and from 1.4 to 2.2 μs for the latter one. If we use our previously recommended values[29] of $K_1 = 5 \times 10^{-32}$ cm^6 s^{-1} and $K_2 = 2 \times 10^{-32}$ cm^6 s^{-1}, the corresponding results become 4.4 and 2.1 μs, respectively, and the difference become smaller. The discrepancies, however, might suggest again the contributions of other loss processes of metastable atoms.

Figure 11 shows the logarithmic plots of the total number of $Kr^*(1s_4)$ resonance atoms corresponding to the data given in Fig. 9 for the metastable atoms, although the selected values of V_s are slightly different. The characteristic feature of the discharge delay is the same for the data in both figures. However, the peak numbers of $Kr^*(1s_4)$ atoms are less than those of $Kr^*(1s_5)$ atoms. Accordingly, the decay time constant is much shorter as 0.62 μs for the 20% case and 0.51 μs for the 40% case. The corresponding data for the total number of $Xe^*(1s_4)$ atoms measured in the Xe(5%) and Xe(10%) panels are shown in Fig. 12. The decay time constants are 0.81 μs for the 5% case and 0.78 μs in the 10% case.

In the estimation of the decay time constants for the resonance atoms, we have to consider both the effective transition probability of the imprisoned radiation and the decay

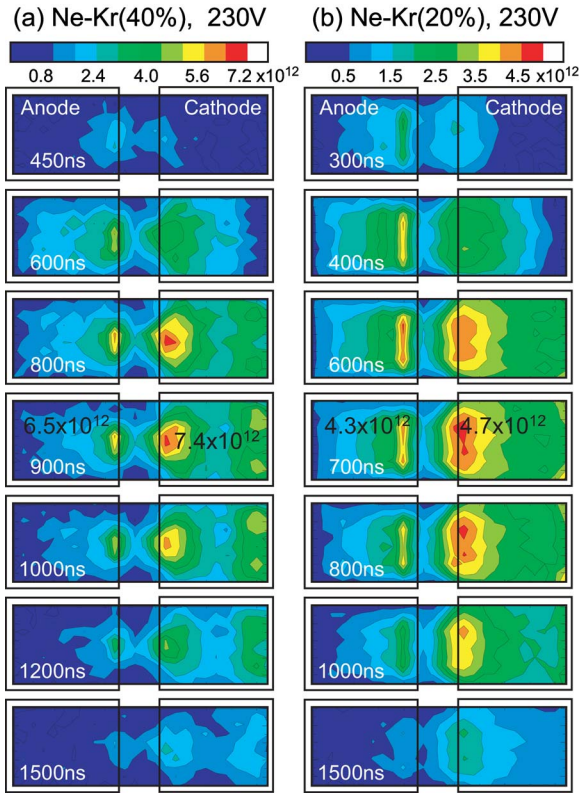

FIG. 7. (Color online) Spatiotemporal behavior of resonance $Kr^*(1s_4)$ atom density (in units of 10^{12} cm^{-3}) measured in (a) Ne–Kr(40%) and (b) Ne–Kr(20%) panels at a sustain pulse voltage of 230 V in a half cycle where the left side is working as the anode and the right side as the cathode.

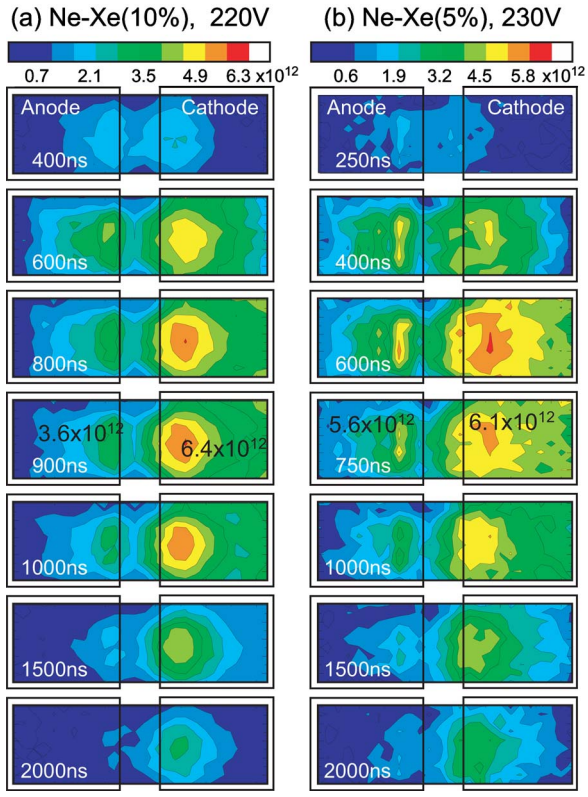

FIG. 8. (Color online) Spatiotemporal behavior of metastable $Xe^*(1s_4)$ atom density (in units of 10^{12} cm^{-3}) measured in (a) Ne–Xe(10%) panel at a sustain pulse voltage of 220 V and (b) Ne–Xe(5%) panel at a sustain pulse voltage of 230 V in the same situation as in Fig. 7.

rate due to the three-body collisions. The apparent radiative decay time constant τ_a of the resonance radiation is given by the following equation:[2,38]

$$\frac{\tau_r}{\tau_a} = \frac{1.15}{\sqrt{3\pi^2 L/\lambda_0}}, \tag{7}$$

provided that the line profile is well broadened by the pressure broadening effect. Here, L(=150 μm) is the rib thickness taken as the minimum dimension of the cell and τ_r (=3.21 ns for Kr and 3.56 ns for Xe)[39] is the radiative lifetime without the trapping effect. Thus, the effective lifetime was calculated to be 0.57 μs for the 123.6 nm line of Kr. The three-body collision rate constants K_1 and K_2 for the $Kr^*(1s_4)$ atoms corresponding to the two reaction channels (1) and (2) are given in Ref. 23 as 4.53×10^{-32} and 1.74×10^{-32} cm^6 s^{-1}, respectively. By using those rate constants, the collisional decay rate becomes 9.64×10^5 and 2.40×10^6 s^{-1}, and the overall lifetime is estimated to be 0.35 and 0.23 μs for the Kr concentration of 20% and 40%, respectively. Those values, however, are smaller than our experimental data. Possible reasons may be attributed to the rough estimation of effective lifetime of the imprisoned radiation by Eq. (7), the contribution of excitation transfer from the $1s_5$ to $1s_4$ levels by two-body collisions and/or the ambiguity in the three-body rate constants.

Similarly, we can estimate the effective decay time constants for the $Xe^*(1s_4)$ atoms. From Eq. (7) the radiative lifetime was calculated as 0.54 μs for the 147.0 nm line of

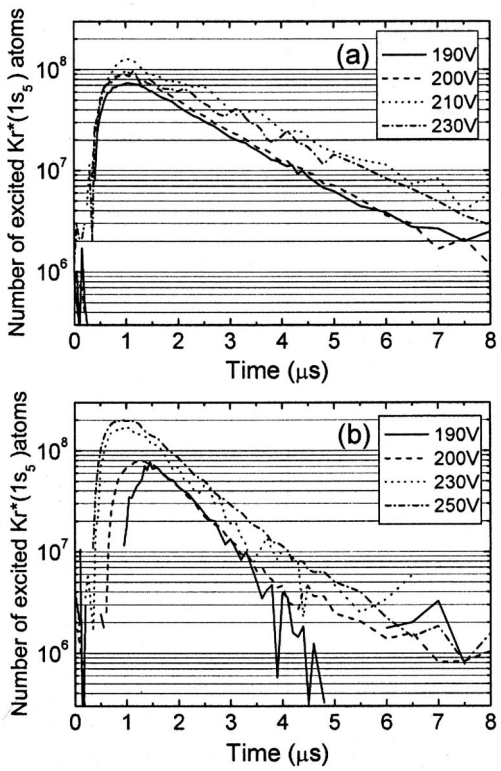

FIG. 9. Temporal behavior of the total number of metastable $Kr^*(1s_5)$ atoms in the unit cell measured in (a) Ne–Kr(20%) panel and (b) Ne–Kr(40%) panel at several values of the sustain voltage.

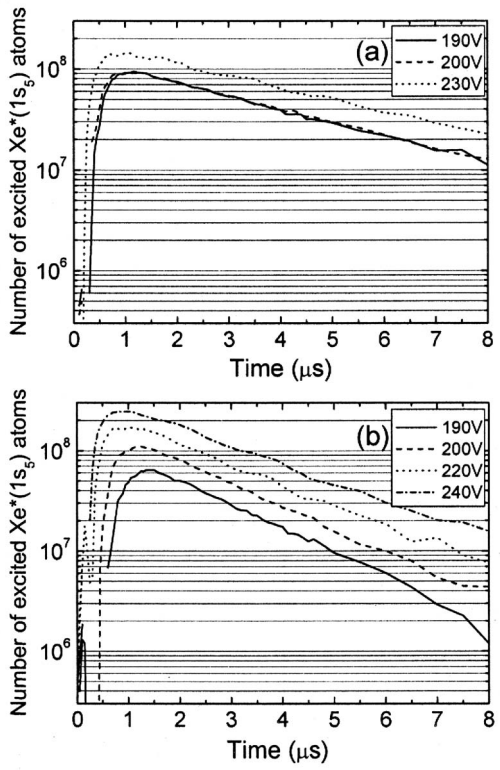

FIG. 10. Temporal behavior of the total number of metastable $Xe^*(1s_5)$ atoms in the unit cell measured in (a) Ne–Xe(5%) panel and (b) Ne–Xe(10%) panel at several values of the sustain voltage.

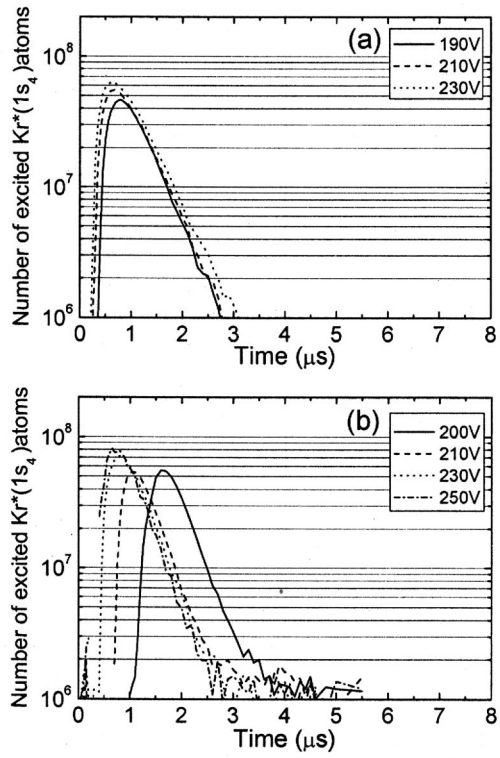

FIG. 11. Temporal behavior of the total number of resonance $Kr^*(1s_4)$ atoms in the unit cell measured in (a) Ne–Kr(20%) panel and (b) Ne–Kr(40%) panel at several values of the sustain voltage.

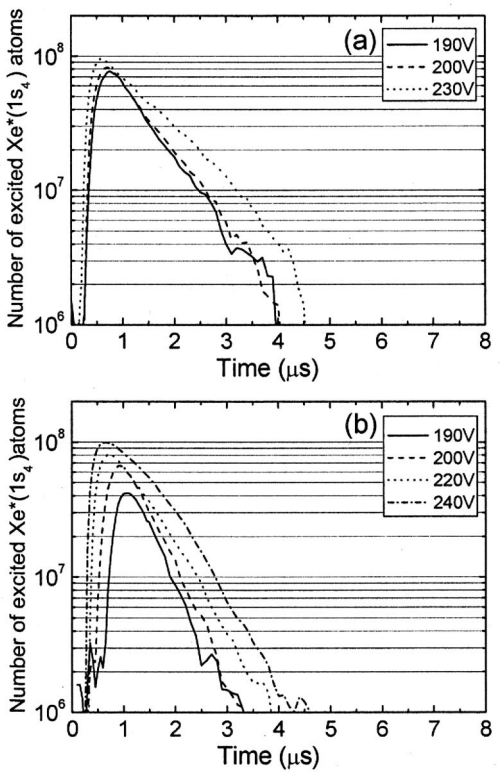

FIG. 12. Temporal behavior of the total number of resonance $Xe^*(1s_4)$ atoms in the unit cell measured in (a) Ne–Xe(5%) panel and (b) Ne–Xe(10%) panel at several values of the sustain voltage.

Xe. As for the three-body collisional rate constants, there are reported values as $K_1=1.55\times10^{-31}$ cm^6 s^{-1} and $K_2=4.07\times10^{-32}$ cm^6 s^{-1}.[36] Thus, the overall lifetime becomes 0.43 and 0.34 μs for the Xe concentration of 5% and 10%, respectively. Again, it is seen that the experimental data are much larger than the estimated values probably due to the same reasons as above.

C. Production efficiency of excited atoms

In order to estimate the production efficiency of excited atoms and VUV photons, the input energy into unit discharge cell P_{in} was derived by integrating the discharge (conduction) current I and multiplying with the sustain voltage V_s. Figure 13(a) shows some examples of the discharge current wave form measured at $V_s=200$ V and Fig. 13(b) shows the input power per cell in a half cycle estimated for the four test panels as a function of V_s. It is seen that the input power increases almost linearly with V_s in all panels.

For the estimation of the production efficiency of excited atoms leading to the VUV emissions, the data shown in Figs. 10–12 should be normalized not only by the input energy P_{in} but also by the decay rate γ. The rate equation for the space-and-time-dependent density of metastable or resonance atoms $n^*(\mathbf{r},t)$ is written as

$$\frac{dn^*(\mathbf{r},t)}{dt}=G(\mathbf{r},t)-L(\mathbf{r},t)=k_e(\mathbf{r},t)n_e(\mathbf{r},t)N_0-n^*(\mathbf{r},t)\gamma, \tag{8}$$

where G is the generation term and L is the loss term. Here, G includes all the production processes by electrons excited

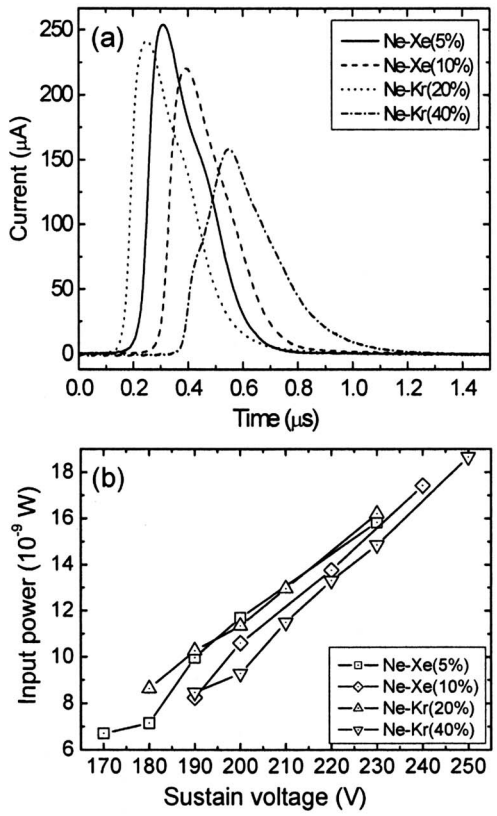

FIG. 13. (a) Wave forms of the discharge current per unit cell measured in the four test panels at the same sustain pulse voltage of 200 V and (b) the estimated input power in a half period as a function of the sustain pulse voltage.

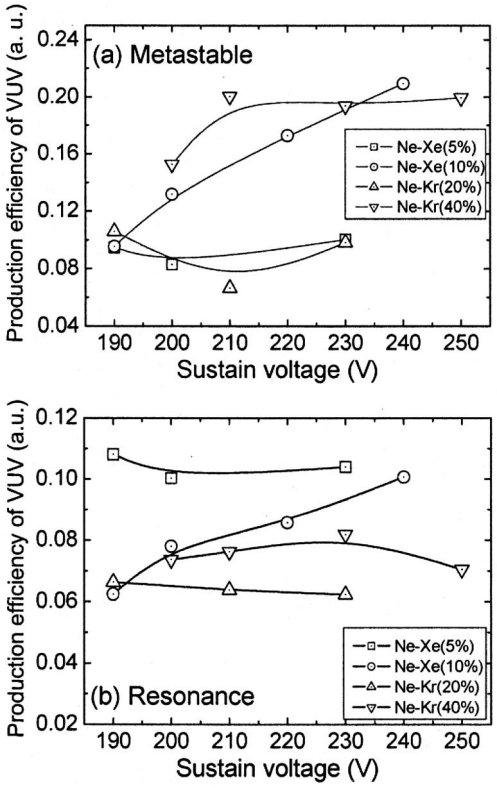

FIG. 14. Production efficiency of VUV photons from (a) metastable atoms and (b) resonance atoms in the four test panels plotted as a function of the sustain pulse voltage.

directly and indirectly via radiative cascades from higher-lying levels with the effective rate constant k_e. It is proportional to the electron density n_e and the number of Kr or Xe atoms in the ground state N_0. Integrating this equation in the half period $T/2$, we can get the total number of production events per unit volume Γ in the period as

$$0 = \left[\int n^*(\mathbf{r},t)dV \right]_0^{T/2} = \Gamma V - \gamma L \int_0^{T/2} \int_S \bar{n}^*(x,y,t)dxdydt, \tag{9}$$

where L is the thickness of the cell along the line of sight (z direction) and $\bar{n}^*(x,y,t)$ is the average density over L. The spatial integration is taken over the whole cell area S in the xy plane. Thus, the quantity

$$\eta \equiv \frac{\Gamma V}{P_{\text{in}}} = \frac{\gamma L}{P_{\text{in}}} \int_0^{T/2} \int_S \bar{n}^*(x,y,t)dxdydt = \frac{\gamma}{P_{\text{in}}} \int_0^{T/2} N^*(t)dt \tag{10}$$

gives the total production efficiency of the excited atoms per unit input energy in the whole volume V of a cell.

The final results are plotted in Figs. 14(a) and 14(b) for the production efficiency of VUV photons from the metastable atoms and the resonance atoms, respectively, estimated for the four test panels as a function of the sustain voltage V_s. It is interesting to see in Fig. 14(a) that the values and the dependence of the production efficiency on V_s are similar in both the Xe(5%) and Kr(20%) cases. However, in the cases of Xe(10%) and Kr(40%), the dependence on V_s looks quite different each other; the behavior of Xe(10%) shows an increasing tendency with V_s in contrast to the nearly constant behavior of the Kr(40%). We have no good explanation on these different dependencies on V_s at the moment, but the saturating tendency in the Kr(40%) case might be due to the electronic quenching of the excited atoms caused by possibly higher electron density at the large Kr concentration. In any case, it can be said that, in both cases of Kr- and Xe-containing panels, the efficiency increases with the concentration of Kr and Xe. It is noted in Fig. 14(b) that the similar trend holds in the dependence on V_s for all cases as in Fig. 14(a), except at very large values of the Xe(5%) data. This is due to the different contribution of three-body collision processes to the quenching of the resonance atoms in each case. In general, the contribution enhances with the increase in the concentration of Kr or Xe in Ne.

Figure 15 shows the overall production efficiency of VUV photons in each gas mixture yielded as the sum of the contributions from both the resonance and metastable atoms for the atomic line and the excimer band. There appears some difference in the efficiency between the Kr(20%) and Xe(5%) cases due to the different contribution of the resonance atoms. Actually, it is seen from Fig. 14 that the contribution of the 147 nm line is comparable to the excimer

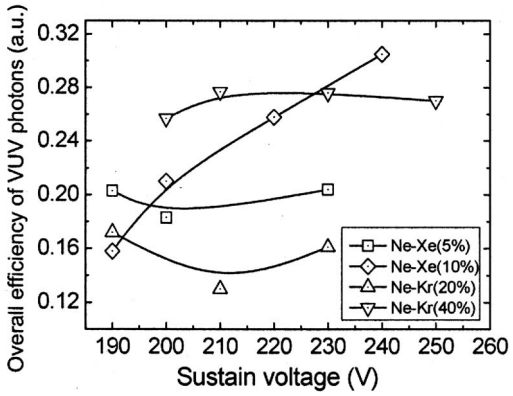

FIG. 15. Overall production efficiency of VUV photons from metastable and resonance atoms in the four test panels plotted as a function of the sustain pulse voltage.

band at 173 nm in the Xe(5%) panel, while the latter contribution becomes larger by about two times in the Xe(10%) panel. On the other hand, in Kr-containing panels, the latter contribution is always larger than the former contribution since we have used relatively high Kr concentrations in this work. Due to this fact, the major VUV emission from Ne–Kr mixture occurs at the 148 nm band, recovering the disadvantage for the phosphor excitation efficiency mentioned in the Introduction. In any case, it was shown that the overall production efficiency of the Ne–Kr(40%) panel was comparable to (or better than at lower V_s) that of the Ne–Xe(10%) panel.

Finally, we will make a comparison of the present measurements with our previous experimental results on the visible emission (full-white state) obtained with practical phosphor-coated panels in the relative scales. As seen in Fig. 16, the intensities of VUV photons estimated from the present measurements are in good agreements with the visible emission data on the V_s dependence and also on the concentration dependence of Kr (or Xe) gas, although the present operating range of V_s is larger by 30 to 40 V due to the differences in structures and operating conditions. Therefore, we believe that the mechanisms causing differences in the emission efficiency in realistic PDP discharge cells have been made clear from the atomistic viewpoint in the present work.

IV. CONCLUSIONS

The spatiotemporal behaviors of the excited Kr^* atoms in the metastable $(1s_5)$ and resonance $(1s_4)$ states were measured in ac-type PDP panels filled with Ne–Kr mixtures of high (20% and 40%) Kr concentrations at a total pressure of 450 Torr. The numbers of $Kr^*(1s_5, 1s_4)$ atoms produced in unit discharge cell are apparently smaller than those of $Xe^*(1s_5, 1s_4)$ atoms measured in lower (5% and 10%) Xe concentration panels with the same total pressure. However, when the difference in the decay rate of excited atoms is taken into account for the estimation of the production efficiency, the result suggests that the Ne–Kr mixture is comparable to the Ne–Xe mixture at the higher Kr concentration used here. It is also estimated that the contribution of the atomic resonance line is smaller than the excimer band under the high-concentration conditions.

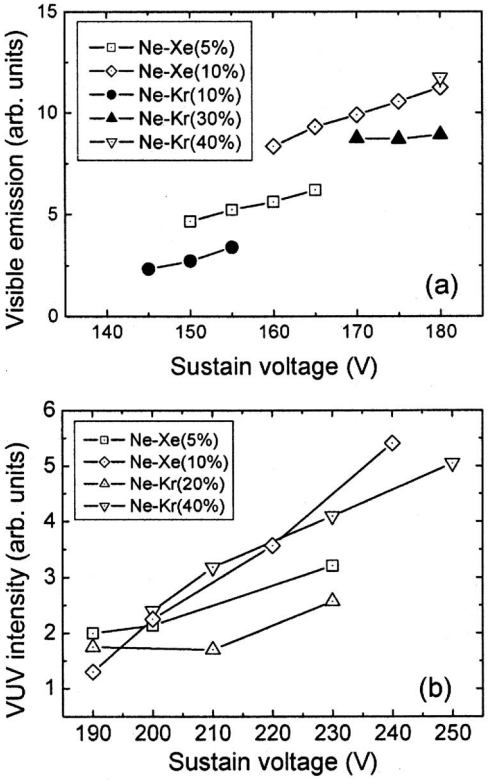

FIG. 16. A comparison of the relative emission efficiency between (a) measured data with phosphor-coated panels and (b) present results estimated from excited atom densities plotted as a function of the sustain voltage.

In practice, however, the wavelengths of VUV emissions at the atomic line and the excimer band in the Ne–Kr system shift to shorter sides than in the Ne–Xe system as mentioned in the Introduction. Therefore, the wavelength dependence of the conversion efficiency of phosphors must be taken into account in the comparison of the luminous efficiency for the use in real plasma display panels.

ACKNOWLEDGMENTS

This work has been partially supported by the SAIT Global Partner Project from Samsung Advanced Institute of Technology and also by the Grants-in-Aid for Scientific Research on the Priority Area of Microplasmas from the Japanese Ministry of Education, Culture, Sports, Science and Technology.

[1] J. P. Boeuf, J. Phys. D **36**, R53 (2003).
[2] J. Meunier, Ph. Belenguer, and J. P. Boeuf, J. Appl. Phys. **78**, 731 (1995).
[3] S. Hashiguchi and K. Tachibana, Jpn. J. Appl. Phys., Part 1 **40**, 1448 (2001).
[4] G. J. M. Hagelaar, M. H. Klein, R. J. M. M. Snijkers, and G. M. W. Kroesen, J. Appl. Phys. **89**, 2033 (2001).
[5] M. F. Gillies and G. Oversluizen, J. Appl. Phys. **91**, 6315 (2002).
[6] W. G. Lee, M. Shao, J. R. Gottschalk, M. Brown, and A. D. Compaan, J. Appl. Phys. **92**, 682 (2002).
[7] W. J. Chung, B. J. Shin, T. J. Kim, H. S. Bae, J. H. Seo, and K. W. Whang, IEEE Trans. Plasma Sci. **31**, 1038 (2003).
[8] J. C. Ahn, T. Y. Kim, J. J. Ko, Y. Seo, G. S. Cho, and E. H. Choi, J. Appl. Phys. **87**, 8045 (2000).
[9] J. H. Seo, H. S. Jeong, J. Y. Lee, C. K. Yoon, J. K. Kim, and K. W. Whang, J. Appl. Phys. **88**, 1257 (2000).
[10] B. K. Min, S. H. Lee, and H. G. Park, J. Vac. Sci. Technol. A **18**, 349 (2000).

[11]G. Veronis, U. S. Inan, and V. P. Pasko, IEEE Trans. Plasma Sci. **28**, 1271 (2000).
[12]T. W. Kim, S. U. Kwon, H. J. Hwang, and M. S. Son, J. Korean Phys. Soc. **42**, S848 (2003).
[13]G. Oversluizen, M. Klein, S. de Zwart, S. van Heuden, and T. Dekker, J. Appl. Phys. **91**, 2403 (2002).
[14]A. Lacoste, L. Tessier, D. Gagnot, and H. Doyeux, *Proceeding of the Tenth International Display Workshop (IDW'03), Fukuoka, 3–5 December 2003* (Society for Information Display, Tokyo, 2003), p.1013.
[15]S.-H. Son, Y.-S. Park, S.-C. Bae, and S.-Y. Choi, Appl. Phys. Lett. **80**, 1719 (2002).
[16]M.-H. Nam, J.-M. Kim, and S.-Y. Choi *et al.*, J. Appl. Phys. **96**, 993 (2004).
[17]Y. Shintani, J. C. Ahn, K. Tachibana, N. Kosugi, and T. Sakai, J. Phys. D **36**, 2928 (2003).
[18]E. H. Choi *et al.*, Appl. Phys. Lett. **81**, 3341 (2002).
[19]M. Noborio, T. Yoshioka, Y. Sano, and K. Nunomura, SID Int. Symp. Digest Tech. Papers **25**, 727 (1994).
[20]H. Hatanaka, Y. M. Kim, G. Y. Kim, H. B. Park, J. H. Hong, Y. J. Lee, W. T. Lee, and J. W. Lee, *Proceeding of the Seventh International Display Workshop (IDW'01), Nagoya, 16–19 October 2001* (Society for Information Display, Tokyo, 2001), p. 1759.
[21]H. Hatanaka, G. Y. Kim, Y. M. Kim, H. B. Park, S. J. Im, J. H. Hong, and Y. J. Lee, SID Int. Symp. Digest Tech. Papers **33**, 852 (2002).
[22]Y. M. Kim *et al.*, *Proceeding of the Eurodisplay 2002, Nice, 1–4 October 2002* (Society for Information Display, Tokyo, 2002), p. 57.
[23]K. Aouame, V. Destombes, H. Brunet, J. Galy, Ph. Guillot, and L. Roubi, J. Phys. B **31**, 4929 (1998).
[24]K. Tachibana, N. Kosugi, and T. Sakai, Appl. Phys. Lett. **65**, 935 (1994).
[25]K. Tachibana, S. Feng, and T. Sakai, J. Appl. Phys. **88**, 4967 (2000).
[26]D. A. Jackson, J. Opt. Soc. Am. **69**, 503 (1979).
[27]A. C. G. Mitchel and M. W. Zemansky, *Resonance Radiation and Excited Atoms* (Cambridge University Pres, London, 1971).
[28]T. Tamida, S. J. Sanders, and M. Tanaka, Jpn. J. Appl. Phys., Part 1 **39**, 583 (2000).
[29]K. Tachibana, S. Kawai, H. Asai, N. Kikuchi, and S. Sakamoto, J. Phys. D **38**, 1739 (2005).
[30]K. Tachibana, K. Mizokami, N. Kosugi, and T. Sakai, IEEE Trans. Plasma Sci. **31**, 68 (2003).
[31]J.-C Ahn, Y. Shinatani, K. Tachibana, T. Sakai, and N. Kosugi, Appl. Phys. Lett. **82**, 3844 (2003).
[32]R. Turner, Phys. Rev. **158**, 121 (1967).
[33]H. Jassens, M. Vanmarcke, E. Desoppere, J. Lenaerts, R. Bouciqué, and W. Wieme, J. Chem. Phys. **86**, 492 (1986).
[34]V. O. Papanayn, G. Ts. Nersisyan, S. A. Ter-Avetisyan, and R. K. Tittel, J. Phys. B **28**, 807 (1995).
[35]P. K. Leichner and R. J. Ericson, Phys. Rev. A **9**, 251 (1974).
[36]J. Galy, K. Aouame, A. Birot, H. Brunet, and P. Millet, J. Phys. B **26**, 477 (1993).
[37]P. K. Leichner, K. F. Palmer, J. D. Cook, and M. Thieneman, Phys. Rev. A **13**, 1787 (1976).
[38]T. Holstein, Phys. Rev. **83**, 1159 (1951).
[39]NIST Atomic Spectra Database Data, http:nist.gov.PhysRefData/ASD/index.html